

MOLECULAR AND SYNAPTIC MECHANISMS

Subcellular calcium dynamics during juvenile development in mouse hippocampal astrocytes

Ryota Nakayama,¹ Takuya Sasaki,¹ Kenji F. Tanaka² and Yuji Ikegaya^{1,3}¹Graduate School of Pharmaceutical Sciences, University of Tokyo, Tokyo, Japan²Department of Neuropsychiatry, School of Medicine, Keio University, Tokyo, Japan³Center for Information and Neural Networks, Osaka, Japan**Keywords:** astrocyte, calcium, hippocampus, imaging

Edited by Masanobu Kano

Received 20 April 2015, revised 26 December 2015, accepted 26 January 2016

Abstract

Astrocytes generate calcium signals throughout their fine processes, which are assumed to locally regulate neighbouring neurotransmission and blood flow. The intercellular morphological relationships mature during juvenile periods when astrocytes elongate highly ramified processes. In this study, we examined developmental changes in calcium activity patterns of single hippocampal astrocytes using a transgenic mouse line in which astrocytes selectively express a genetically encoded calcium indicator, Yellow Cameleon-Nano50. Compared with postnatal day 7, astrocytes at postnatal day 30 showed larger subcellular calcium events and a greater proportion of somatic events. At both ages, the calcium activity was abolished by removal of extracellular calcium ions. Calcium events in late juvenile astrocytes were not affected by spontaneously occurring sharp waves that trigger synchronized neuronal spikes, implying the independence of astrocyte calcium signals from neuronal synchronization. These results demonstrate that astrocytes undergo dynamic changes in their activity patterns during juvenile development.

Introduction

Astrocyte Ca²⁺ signals are thought to play important roles in controlling neighbouring synaptic transmission and cerebral blood flow (Attwell *et al.*, 2010; Volterra *et al.*, 2014; Khakh & McCarthy, 2015). Such intercellular interactions are primarily achieved at subcellular processes in which astrocytes tightly enwrap synapses (Bushong *et al.*, 2002; Gordon *et al.*, 2009) and blood vessels (Gordon *et al.*, 2008; Girouard *et al.*, 2010). Most early studies, however, monitored signals only from the cell body or the main processes up to a few micrometres from the soma, due to the difficulty of visualizing the complex morphology of fine astrocytic processes in living tissues (Reeves *et al.*, 2011). This technical limitation might underlie the inconclusive results presented by several studies that challenged the significance of astrocyte Ca²⁺ signals (Fiacco *et al.*, 2009; Agulhon *et al.*, 2010).

Recent advances in high-resolution two-photon imaging techniques (Di Castro *et al.*, 2011; Min & Nevian, 2012) and highly sensitive genetically encoded Ca²⁺ indicators (GECIs) (Shigetomi *et al.*, 2010; Hausteiner *et al.*, 2014; Kanemaru *et al.*, 2014) have begun to overcome previous technical limitations. These studies revealed that astrocytes show asynchronous Ca²⁺ transients among

multiple processes, which are likely to serve as a functional element in the regulation of neighbouring neurotransmission (Volterra *et al.*, 2014).

Despite recent findings for the detailed dynamics of astrocyte processes, evidence is still lacking about the postnatal developmental changes in the spatiotemporal patterns of astrocyte Ca²⁺ signals. From birth to the late juvenile period, astrocytes continue to elaborate highly ramified processes (Bushong *et al.*, 2004), and the expression levels of certain types of functional proteins are up- or down-regulated in astrocytes (Sutherland *et al.*, 1996; Furuta *et al.*, 1997; Nagy *et al.*, 1999; Seifert *et al.*, 2009; Sun *et al.*, 2013). In parallel, neuronal populations in the hippocampus begin to establish dense wiring patterns and generate organized firing patterns, termed sharp wave bursts (Buhl & Buzsáki, 2005), which may affect the functional coupling between astrocytes and neurons (Freeman, 2010).

Based on the research background, the aim of this study was to understand the similarity and difference of the spatiotemporal patterns of astrocyte Ca²⁺ dynamics across different developmental stages. Using a transgenic mouse line in which astrocytes selectively express a GECI, Yellow Cameleon-Nano50 (YC-Nano50) (Horikawa *et al.*, 2010), and a wide-field confocal scanning method, we monitored subcellular activity patterns from the entire structures of single astrocytes in a confocal plane in acute hippocampal slices.

Correspondence: Dr Takuya Sasaki and Dr Yuji Ikegaya, as above.
E-mails: tsasaki@mol.f.u-tokyo.ac.jp and yuji@ikegaya.jp

Materials and methods

Animal ethics

All experiments were performed with the approval of the animal experiment ethics committee at the University of Tokyo (approval number P24-8) and according to the University of Tokyo guidelines for the care and use of laboratory animals.

Transgenic animals

Bigenic mice were obtained by crossing Mlc1-tTA BAC transgenic mice (Tanaka *et al.*, 2010) with tetO-YC-Nano50 *Actb* gene locus knockin mice. Details of the transgenic lines are described elsewhere (Kanemaru *et al.*, 2014). The bigenic mice were not treated with doxycycline.

Hippocampal slice preparation

Acute slices were prepared from the medial to ventral part of the hippocampal formation. Postnatal day 7 to day 30 transgenic mice were anaesthetized with ether and decapitated, and a posterior brain block (400 μm thick) was obliquely cut at an angle of 12.7° in the fronto-occipital direction at a speed of 0.08 mm/s using a vibratome in ice-cold cutting solution consisting of (in mM) 222.1 sucrose, 27 NaHCO₃, 1.4 NaH₂PO₄, 2.5 KCl, one CaCl₂, seven MgSO₄ and 0.5 ascorbic acid, bubbled with 95% O₂ and 5% CO₂ (Mizunuma *et al.*, 2014). This cutting angle preserved more of the Schaffer collaterals. Slices were allowed to recover at 37 °C for at least 2 h, submerged in a chamber filled with oxygenated artificial cerebrospinal fluid (aCSF) composed of (in mM) 127 NaCl, 26 NaHCO₃, 3.5 KCl, 1.24 NaH₂PO₄, 1.2 MgSO₄, 2.4 CaCl₂ and 10 glucose (pH 7.4, 300 mOsm/L).

Hippocampal slice cultures were prepared from postnatal day 7 (P7) transgenic mice. Briefly, mouse pups were chilled, and the brains were removed and horizontally cut into 400- μm -thick slices in aerated, ice-cold Gey's balanced salt solution supplemented with 36 mM glucose. Entorhino-hippocampal stumps were transferred to a 35-mm dish filled with the cold incubation medium composed of 2.3 mM *N*-2-hydroxyethylpiperazine-*N*-2-ethane sulfonic acid (HEPES), 9.1 mM tris(hydroxymethyl)aminomethane (Tris), 60.6% minimal essential medium (MEM) and 30.3% Hanks' balanced salt solution (HBSS), and incubated at 4 °C for 30–90 min. Then the slices were cultivated on Ompipore membrane filters (JHWP02500; Millipore, Billerica, MA, USA) that were laid on plastic O-ring discs. The cultures were fed with 1 mL of culture medium composed of 0.034% NaHCO₃, 75% cold incubation medium, 25% horse serum and 0.1 mg/mL gentamicin sulfate in a humidified incubator at 37 °C in 5% CO₂. The medium was changed every 3.5 days.

In situ calcium imaging of astrocytes

Recordings were performed in a submerged chamber perfused at 2 mL/min with oxygenated aCSF at 35 °C. For experiments to record sharp wave events, the chamber was perfused at 8 mL/min with oxygenated aCSF at 35 °C. After being perfused in a recording chamber with aCSF for >15 min, we initiated the imaging of spontaneous calcium signals from astrocytes in the CA1 stratum radiatum. Unless otherwise specified, the YC-Nano50-positive astrocytes for imaging were selected based on the following criteria: (1) the fluorescence image was completely isolated from other fluorescent cells, and (2) the morphology exhibited ramified processes and did

not show apparent varicose-like structures and swelling on their processes. A laser diode (Stradus 445-80; Vortran Laser Technology, Sacramento, CA, USA) tuned to 445 nm was used for excitation. Cyan and yellow fluorescence signals were acquired with a dichroic mirror (440 nm) and band-pass filters (480/40 nm and 535/30 nm for cyan and yellow fluorescence, respectively). Fluorescence was captured at 1–5 Hz with a pixel size of $0.4 \times 0.4 \mu\text{m}^2$ using an upright microscope with a $1\times$ intermediate magnification lens (ECLIPSE FN1; Nikon, Tokyo, Japan), a Nipkow disc confocal microscopy (CSU-X1; Yokogawa Electric, Tokyo, Japan) and a cooled EM-CCD camera (iXonEM⁺ DV897; Andor Technology, Tokyo, Japan) through a water-immersion objective lens ($\times 40$, 0.8 NA; Nikon).

For bulk loading of YC-Nano50-negative astrocytes, the tip of the pipette (3–5 M Ω) filled with 20 μM Oregon Green 488 BAPTA-1 (OGB-1) AM, 10% dimethyl sulfoxide and 1% Pluronic F-127 was inserted into the CA1 stratum radiatum and a pressure of 50–60 hPa was applied for 5–10 min using a 10-mL syringe pressurizer.

Detection of calcium signals

Slices that moved more than 5 μm in the *Z*-axis were discarded from the following analyses. *X–Y* drifts were automatically *post-hoc* corrected by custom software (MATLAB R2013b; Mathworks, Natick, MA, USA). All images were Gaussian filtered [standard deviation (SD) = 2 pixels] in space and averaged to 1 Hz before the detection procedure. The signal amplitude was expressed as the yellow fluorescent protein (YFP)/cyan fluorescent protein (CFP) fluorescence ratio, *R*. The change in the fluorescence ratio was defined as $\Delta R/R = (R_t - R_0)/R_0$, where *R_t* is the fluorescence ratio at time *t* and *R₀* is the ratio averaged over the bottom 20% of all values for 30 s before and after time *t*. In each pixel, a $\Delta R/R$ value was converted to a *z*-score, defined as the ratio of the difference between $\Delta R/R$ and the average of baseline $\Delta R/R$ to the standard deviation of the baseline $\Delta R/R$; note that the average of the bottom 50% of all $\Delta R/R$ values across the entire recording period in that pixel was regarded as the baseline $\Delta R/R$. In each frame, the *z*-scored image was converted into a binary image by extracting active pixels at a *z*-score threshold of 6. The neighbouring active pixels in space and time were interconnected and defined as a Ca²⁺ event if the total area exceeded 16 μm^2 . For each event, the event area was defined as the maximum intensity projection, and the event duration was defined as the number of frames containing the event.

Extracellular recording and sharp wave detection

The local field potential (LFP) was recorded from the CA1 stratum pyramidale using borosilicate glass pipettes (1 M Ω) filled with aCSF. The signals were amplified by a MultiClamp 700B (Molecular Devices, Sunnyvale, CA, USA), digitized at 20 000 Hz by pCLAMP 9 (Molecular Devices). To detect sharp waves (SPWs), the LFP traces were band-pass filtered at 2–30 Hz and were thresholded at four times above the SD of the baseline noise. The detected SPW events were scrutinized by eye and manually rejected if they were erroneously detected.

Histological analysis

Slices were fixed in 4% paraformaldehyde in 100 mM phosphate-buffered saline (PBS) overnight at 4 °C. Image sections were acquired at a *Z*-depth interval of 2 μm with a two-photon laser-scanning microscope based on a mode-locked Ti:sapphire laser with a

100-fs pulse width, 80-MHz pulse frequency and 900-nm wavelength (Maitai; Spectra Physics, Santa Clara, CA, USA); an upright microscope (BX61 WI; Olympus, Tokyo, Japan); and a water-immersion objective lens (25 \times , 1.05 NA, Olympus). Z-series images were analysed using ImageJ. To calculate astrocyte volume, the contour of YC-Nano50-positive signals was manually defined by eye on each section. The product of two (in μm) by the sum of areas (in μm^2) of all sections was used as the putative volume.

For immunohistochemistry, transgenic mice were perfused with cold 4% paraformaldehyde (PFA) in 25 mM PBS and decapitated. After dissecting the brain, they were placed in fixative in 4% PFA for 30 min, then placed in 30% sucrose in PBS until equilibrated. Frozen coronal sections (40 μm) were cut and the slices were permeabilized in 100 mM PBS with 0.3% Triton X-100 and 10% goat serum at room temperature for 60 min. They were then incubated with primary mouse monoclonal anti-NeuN antibody (1 : 1000; Millipore) and primary rabbit monoclonal anti-glial fibrillary acidic protein (GFAP) antibody (1 : 1000; Sigma, St Louis, MO, USA) for two overnight periods at 4 $^{\circ}\text{C}$ and labelled with secondary anti-mouse IgG Alexa-405 (1 : 500; Invitrogen, Carlsbad, CA, USA) and secondary anti-rabbit IgG Alexa-594 (1 : 500; Invitrogen) overnight at room temperature. Images were acquired at a Z-depth interval of 2 μm using a confocal laser-scanning microscope (CV-1000; Yokogawa Electric) with a water-immersion objective lens ($\times 20$, 0.8 NA).

Statistics

All values are reported as mean \pm SEM. To identify significant differences, we performed a Steel–Dwass test, Mann–Whitney *U*-test and paired *t*-test. In all tests, $P < 0.05$ was considered significant (two-tailed).

Results

Imaging spontaneous Ca^{2+} dynamics in astrocytes during juvenile development

To detect Ca^{2+} events specifically from the astrocyte population, we obtained bigenic Mlc1-tTA::tetO-YC-Nano50 mice by crossing two mouse lines: one in which the expression of a tetracycline-controlled transactivator protein (tTA) is driven by the promoter megalencephalic leukoencephalopathy with subcortical cysts 1 (Mlc1), which has been proven to be astrocyte-specific (Schmitt *et al.*, 2003), and the other in which the tetracycline operator (tetO) drives the expression of YC-Nano50 (Horikawa *et al.*, 2010). We performed immunohistochemical labelling of neurons and astrocytes to confirm the selective expression of the transgene (Fig. 1A, top). No YC-Nano50 signals overlapped with NeuN, a neuron-specific marker. In GFAP-positive astrocytes, we measured green fluorescence intensity, which represents YC-Nano50 expression (Fig. 1A, bottom). A bimodal distribution was revealed with YC-Nano50-positive and YC-Nano50-negative signals at both P7 and P30, indicating that YC-Nano50 fluorescence is separable from the background fluorescence, such as autofluorescence. In the hippocampal CA1 stratum radiatum, 38 \pm 9 and 43 \pm 5% of GFAP-positive astrocytes expressed YC-Nano50 at P7 and P30, respectively. At both ages, the area of GFAP-positive structures did not differ between YC-Nano50-positive and YC-Nano50-negative astrocytes (P7: YC-Nano50-positive, 254 \pm 82 μm^2 , YC-Nano50-negative, 252 \pm 74 μm^2 , Steel–Dwass test, $P > 0.05$; P30: YC-Nano50-positive, 232 \pm 49 μm^2 , YC-Nano50-negative, 207 \pm 54 μm^2 , Steel–Dwass test, $P > 0.05$). To examine the long-term stability of YC-Nano50 expression in astro-

cytes, we cultivated hippocampal slices and conducted time-lapse imaging of YC-Nano50 fluorescence for 1 week (Fig. 1B). Of 62 astrocytes showing YC-Nano50 fluorescence on days *in vitro* (Div) 12 ($n = 3$ pictures), 85.6 \pm 4.5% of cells maintained their expression from Div 4 to 12 (Fig. 1C). Those cells that lost their fluorescence might have died during the cultivation period. In the same images, 14.4 \pm 4.5% of cells newly acquired YC-Nano50 fluorescence. These results demonstrate that a small subset of cells change fluorescence expression during a period of 1 week in the transgenic mouse line. The three-dimensional tracing of YC-Nano50-expressing astrocytes from two-photon image stacks with a section interval of 2 μm revealed that the total volume of single astrocytes at P7 and P30 was 38 950 \pm 5198 μm^3 (calculated from 16.2 \pm 1.3 sections; $n = 5$ cells) and 65 077 \pm 14 100 μm^3 (calculated from 28.8 \pm 4.2 sections; $n = 5$ cells), respectively. Although we note that this volume analysis is a rough estimation as it was performed at low spatial resolution ($\times 25$) in fixed preparations, the result, at least, confirms that YC-Nano50-positive astrocyte volume increases as the animal age increases.

We next confirmed the detectability of astrocyte Ca^{2+} dynamics in response to neuronal stimulation. Using a Nipkow disc confocal microscope, which enables wide-field confocal scanning, we monitored the spatiotemporal patterns of Ca^{2+} activity from the whole territory of a single astrocyte in a confocal plane. Electrical burst stimulation was applied to the Schaffer collateral afferents (250 μA , 50 Hz). Images were captured at a frame rate of 1 Hz. The YC-Nano50 fluorescence traces were expressed as YFP/CFP fluorescence ratios. Under our imaging conditions, YC-Nano50-positive astrocytes showed a detectable increase in their $\Delta R/R$ fluorescence in response to burst stimulation with more than ten pulses (Fig. 1D, $n = 4$). The result confirms that YC-Nano50-positive astrocytes have the ability to respond to intense neuronal activity. To compare the Ca^{2+} fluorescence dynamics of YC-Nano50-positive astrocytes with that of YC-Nano50-negative astrocytes, YC-Nano50-negative astrocytes were labelled with OGB-1 using a bulk-loading method with pressure injection. In the same conditions, tens of pulses were required to evoke an apparent increase in OGB-1 $\Delta F/F$ fluorescence ($n = 4$). This result demonstrates that Ca^{2+} responses detected in YC-Nano50 fluorescence to external stimulation are more sensitive than these in OGB-1 fluorescence.

The technical advancement of recent GECIs raises the new challenge of efficiently extracting prominent signals from sequential images. A conventional region of interest (ROI)-based analysis generally extracts time-varying fluorescence traces from arbitrarily selected ROIs, as shown in Fig. 1E and F, but this method cannot visualize the precise area where fluorescence signals spread. We therefore employed an ROI-free image analysis to systematically detect significant Ca^{2+} events (Asada *et al.*, 2015). This analysis is mathematically simple with fewer subjective criteria and helps us to recognize processed data more intuitively with single-pixel resolution because the converted movie keeps the same movie structures as those of the original. In each frame, a $\Delta R/R$ image was converted to a z-scored image and then converted into a binary image at a z-score threshold of 6 (Fig. 1G). The neighbouring active pixels in space and time were interconnected. A Ca^{2+} event is defined if the maximum area in a frame is at least 16 μm^2 (100 pixels).

Astrocytes in late juvenile age more frequently exhibit large Ca^{2+} events

As shown in Fig. 2A, a single astrocyte generated various repertoires of Ca^{2+} events in both the soma and processes. During an

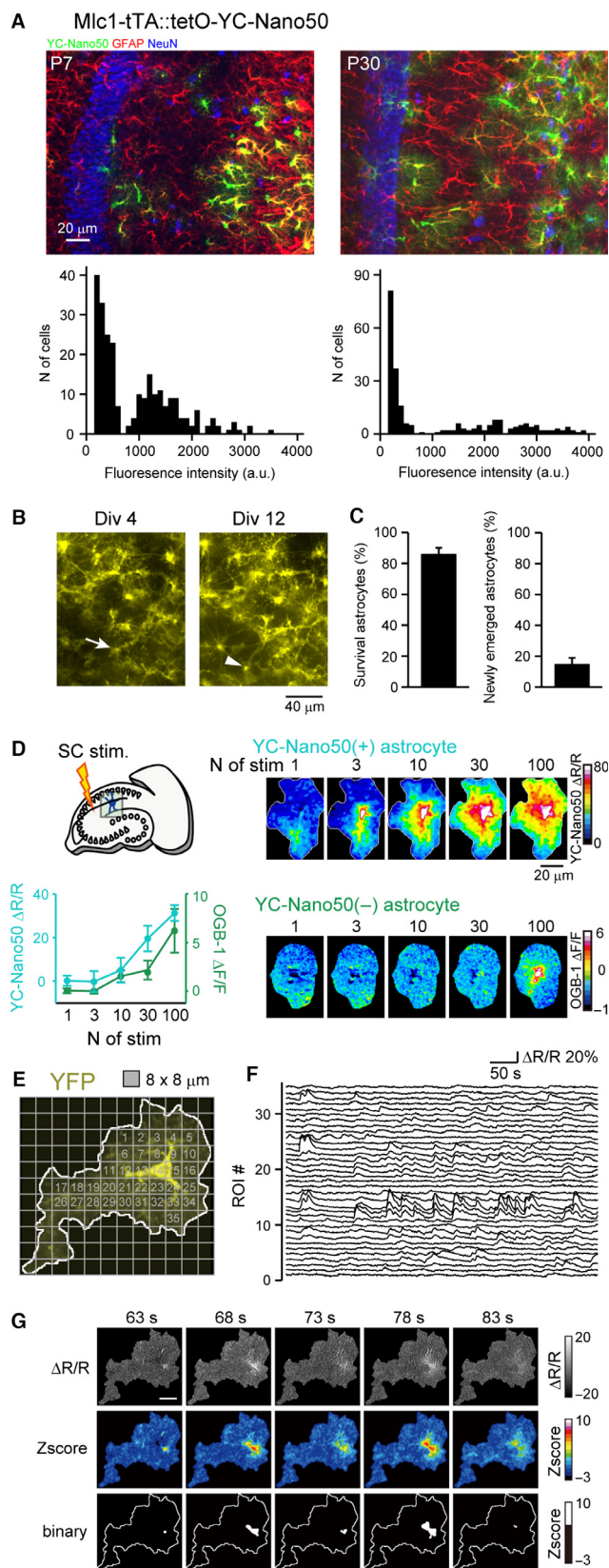


FIG. 1. Detection of localized Ca^{2+} events in single hippocampal astrocytes in Mlc1-tTA::tetO-YC-Nano50 mice. (A) (top) NeuN-stained neurons, GFAP-stained astrocytes and YC-Nano50-expressing astrocytes in the stratum radiatum of the hippocampal CA1 area. (bottom) Distribution of green fluorescent intensity of GFAP-positive astrocytes, showing a bimodal distribution with YC-Nano50-positive cells located >700 and YC-Nano50-negative cells located <700 . The arrows indicate the threshold for separating the two cell groups. (B) Representative YC-Nano50-positive astrocytes at 4 and 12 days *in vitro* (Div) in a cultured hippocampal slice prepared from a P7 transgenic mouse. (C) The percentage of astrocytes that showed YC-Nano50 expression at both Div 4 and Div 12 (left) and the percentage of astrocytes that showed YC-Nano50 expression at Div 12 but not at Div 4 (right) in Div 12 astrocytes. The arrow shows an astrocyte that disappeared at Div 12. The arrowhead shows an astrocyte that newly expressed YC-Nano50 at Div 12. (D) Imaging of Ca^{2+} activity of a single astrocyte in response to Schaffer collateral (SC) electrical burst stimulation with a frequency of 50 Hz. YC-Nano50 $\Delta R/R$ and OGB-1 $\Delta F/F$ images were obtained from a YC-Nano50-positive and an OGB-1-labelled YC-Nano50-negative astrocyte, respectively (right). Numbers indicated above represent the number of pulses. (left) $\Delta R/R$ and $\Delta F/F$ fluorescence changes in YC-Nano50-positive and YC-Nano50-negative astrocytes are plotted against the number of stimulus pulses ($n = 4$). (E) Confocal image of a YC-Nano50-expressing astrocyte in the stratum radiatum of the hippocampal CA1 area overlaid with ROIs (grey) put along the image arranged in a reticular pattern. The contour of the astrocyte is indicated by the white outline. (F) Representative fluorescence traces of spontaneous astrocyte Ca^{2+} activity observed from the 35 ROIs shown in E. (G) ROI-free image analysis. Times indicated represent times after start of imaging. Sequential $\Delta R/R$ images (top) were converted to z-scored images (middle) shown as the signal amplitude expressed as SD multiples above the mean baseline calculated in each pixel. The binary image was obtained by detecting significant pixels by crossing a z-score threshold of 6 (bottom).

observation period of 9.5 ± 0.4 , 15.1 ± 1.7 and 9.1 ± 0.5 min, 31.7 ± 6.0 , 50.0 ± 14.9 and 51.7 ± 9.0 events emerged in a single astrocyte at P7 ($n = 24$ slices from 13 animals), P18 ($n = 8$ slices from three animals) and P30 ($n = 23$ slices from 15 ani-

mals), respectively. To examine whether individual subcellular Ca^{2+} events are synchronized in each frame within an astrocyte, we analysed the time changes in the number of events and the total size of events per frame (Fig. 2B and C, left). Each graph was collapsed into a frequency distribution (Fig. 2B and C, middle), and the standard deviation (SD) of the distribution was measured. In the example data shown in Fig. 2B and C, the SDs of the frequency and the total size were 0.63 and 60.6, respectively. To estimate the chance level of the SD, surrogate datasets were created in each movie by randomly shuffling onset frames of individual events. This procedure collapses temporal correlations between events but preserves the number of total events, as well as the duration and size of individual events. The average SD at chance level was obtained by creating 100 surrogate datasets. In P7, P18 and P30 mice, no significant differences in the SDs of the number and total size of events were found between real and surrogate datasets (Fig. 2B, right, number of events: P7, $t_{23} = 1.33$, $P = 0.20$, P18, $t_8 = 0.83$, $P = 0.43$, P30, $t_{22} = 0.90$, $P = 0.38$; Fig. 2C, right, total event size: P7, $t_{23} = 0.91$, $P = 0.37$, P18, $t_8 = 0.07$, $P = 0.94$, P30, $t_{22} = 0.47$, $P = 0.64$). These results suggest that subcellular Ca^{2+} events occur asynchronously in a single astrocyte. The size of individual astrocyte Ca^{2+} events varied by over two orders of magnitude. The frequency of total Ca^{2+} events per $1000 \mu\text{m}^2$ did not differ among the three juvenile ages (Fig. 2E, left; Steel–Dwass test, $P > 0.05$). The frequencies of large Ca^{2+} events with a size of more than $100 \mu\text{m}^2$ were significantly higher in P18 and P30 astrocytes than in P7 astrocytes (Fig. 2D and E, right; Steel–Dwass test, P7 vs. P18, $P < 0.05$; P7 vs. P30, $P < 0.05$). In P7, P18 and P30 astrocytes, 42.3 ± 2.2 , 35.3 ± 3.1 and $40.2 \pm 2.2\%$ of Ca^{2+} events had a duration shorter than 1 s whereas 14.6 ± 2.6 , 20.4 ± 1.3 and $8.3 \pm 1.7\%$ of Ca^{2+} events had a duration longer than 10 s, respectively (Fig. 2F; Kolmogorov–Smirnov post-hoc test with Bonferroni correction, P7 vs. P18, $P = 0.013$; P7 vs. P30, $P = 1.00$; P18 vs. P30, $P = 0.0036$).

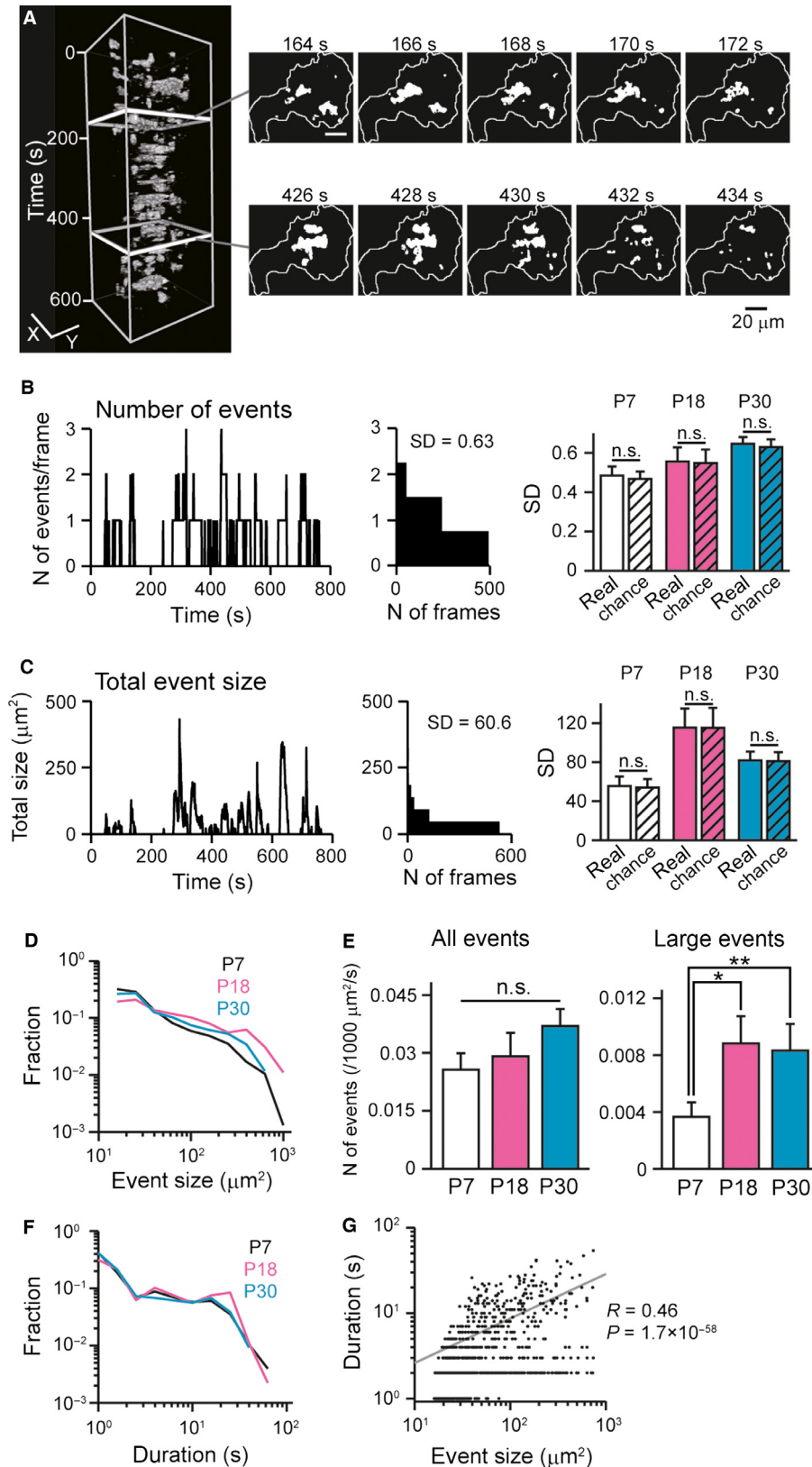


FIG. 2. Developmental changes in astrocyte Ca^{2+} signals during juvenile periods. (A) (left) Representative Ca^{2+} events in an astrocyte during a 10-min recording period. The depth axis represents time starting from the top. Focused frames are magnified in the right panels. (B) (left) The number of Ca^{2+} events observed in a frame. The right histogram shows the distribution of the number of events. The SD was calculated to be 0.63. (right) Comparison of SDs between real and surrogate data sets. Paired *t*-test, $P > 0.05$. (C) Same as in B, but plotted for total event size. (D) Distribution of Ca^{2+} event size in P7, P18 and P30 astrocytes. (E) Average frequencies of all events and events with a size $>100 \mu\text{m}^2$. Steel-Dwass test, $P > 0.05$, $*P < 0.05$, $**P < 0.01$. (F) Same as in D, but plotted for event duration. (G) Relationship between size and duration of individual Ca^{2+} events. $R = 0.46$, $P = 1.7 \times 10^{-58}$.

The average duration was 4.9 ± 0.4 , 6.4 ± 0.4 and 5.3 ± 0.3 s in P7, P18 and P30 astrocytes, respectively. There was a significant correlation between event size and duration, showing that larger events lasted for longer periods (Fig. 2G; $n = 1103$ events, $R = 0.46$, $P = 1.7 \times 10^{-58}$).

Difference of spatial distribution of astrocyte Ca^{2+} events in early and late juvenile mice

As shown by Tang *et al.* (2015), the dynamics of Ca^{2+} signals in astrocytic processes are different from those in the soma. We compared the spatial features of astrocyte subcellular Ca^{2+} events among the three postnatal ages. For each event, an overlap rate with the soma was defined as the ratio of the size of the signal area that overlapped with the somatic region to the entire signal size (Fig. 3A). Ca^{2+} events with an overlap rate of more than 50% and <20% were defined as events at the soma and the process, respectively. As shown in the cumulative distribution of the overlap rate

in Fig. 3B, 5.8, 4.6 and 13.4% of Ca^{2+} events were classified as somatic events whereas 83.5, 88.3 and 74.9% of Ca^{2+} events were classified as events at processes in P7, P18 and P30 astrocytes, respectively. The absolute event frequency of somatic events in P30 astrocytes was significantly higher than that in P7 astrocytes (Steel–Dwass test, $P < 0.05$). These results suggest that astrocyte Ca^{2+} events become more concentrated on the somatic region during juvenile development.

Although the majority of overall Ca^{2+} events arise from astrocyte processes, the frequency of events in a given pixel appeared higher in the somatic area. To define the preferential sites of Ca^{2+} activity, all binary images in a movie were superimposed, and the stacked image was converted into a z-scored image (Fig. 3D). The pixels with a z-score of more than 2 were defined as a hotspot area. At all ages, the occupancy rate of a hotspot area in the somatic region was significantly higher than that in the process region (Fig. 3E; paired *t*-test, P7, $t_{23} = 3.21$, $P = 0.0039$; P18, $t_8 = 3.67$, $P = 0.0063$; P30, $t_{22} = 4.92$, $P = 6.4 \times 10^{-5}$).

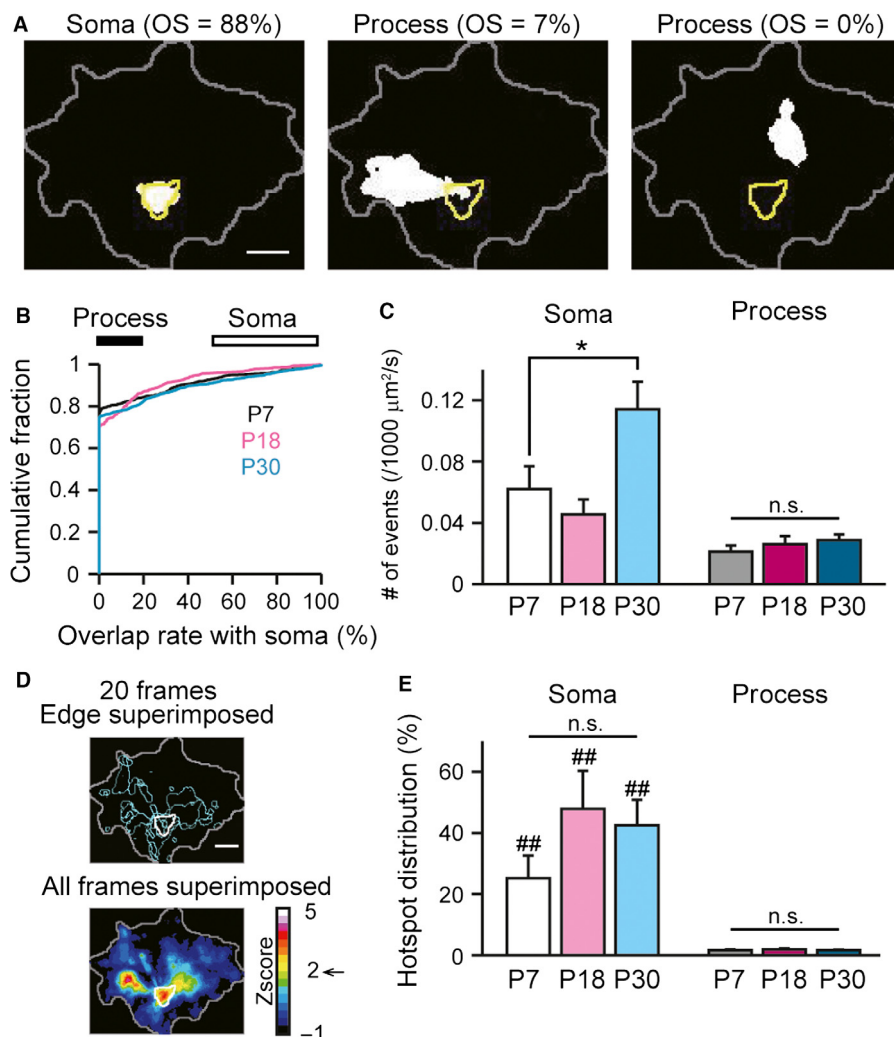


FIG. 3. Location of astrocyte Ca^{2+} events. (A) Three representative Ca^{2+} events are shown. The contour of the astrocytic territory and the soma are shown by the grey and yellow lines, respectively. In each event, the ratio of the signal area overlapped with the soma to the total signal area was defined as an “overlap rate with soma (OS)”. (B) Distribution of overlap ratios with soma. (C) Average frequencies of Ca^{2+} events at soma and processes. Steel–Dwass test, $*P < 0.05$. (D) Hotspots of astrocyte Ca^{2+} events. (left) Contours of Ca^{2+} events observed in 20 representative frames were superimposed. The somatic region is shown by the white line. (right) The number of active frames in a single 10-min movie in individual pixels was superimposed and shown as a z-scored image. The hotspot area was defined as pixels with a z-score of more than 2 (arrow). Scale bar = 10 μm . (E) The occupancy ratio of hotspots in soma and process at individual ages. Paired *t*-test, soma versus process at individual ages, ## $P < 0.01$. Steel–Dwass test across ages, $P > 0.05$.

Mechanisms underlying astrocyte Ca^{2+} events in early and late juvenile stages

To examine the mechanisms underlying astrocyte Ca^{2+} dynamics, we next performed pharmacological experiments; we applied 125 μM MCPG, a group I and II metabotropic glutamate receptor antagonist, 100 μM suramin, a broad purinergic receptor antagonist, and 50 μM HC030031, a transient receptor potential ankyrin-1 (TRPA1) channel antagonist. In either P7 or P30 mice, none of these inhibitors affected the frequency of either all or large Ca^{2+} events, except that suramin significantly increased the frequency of large Ca^{2+} events with a size of more than 100 μm^2 in P7 astrocytes (Fig. 4A and B; P7 all events: MCPG, $t_5 = 0.37$, $P = 0.73$, suramin, $t_4 = -1.54$, $P = 0.20$, HC030031, $t_4 = -1.11$, $P = 0.33$; P30 all events: MCPG, $t_3 = 0.80$, $P = 0.48$, suramin, $t_3 = -1.81$, $P = 0.17$, HC030031, $t_5 = -0.29$, $P = 0.79$; P7 large events: MCPG, $t_5 = -0.55$, $P = 0.61$, suramin, $t_4 = -5.16$, $P = 0.0067$, HC030031, $t_4 = -1.27$, $P = 0.27$; P30 large events: MCPG, $t_3 = 0.77$, $P = 0.50$, suramin, $t_3 = -1.09$, $P = 0.35$, HC030031, $t_5 = 1.03$, $P = 0.35$, paired t -test). These results suggest that activation of metabotropic glutamate receptors, purinergic receptors or TRPA1 channels does not modulate the entire frequency of astrocyte Ca^{2+} activity. In Ca^{2+} -free aCSF, the frequency of Ca^{2+} events was significantly reduced at both ages (Mann–Whitney U -test, P7 all events: $P = 0.015$; P30 all events: $P = 0.0024$; P7 large events: $P = 0.14$; P30 large events: $P = 0.0023$), suggesting that extracellular Ca^{2+} influx is a major source of the astrocyte Ca^{2+} events, although further mechanisms remain to be identified.

We next analysed whether these blockers affect subcellular activity (Fig. 4C). Of all the drugs tested, only application of HC030031 caused a significant reduction in Ca^{2+} events specifically at the somatic region in P30 mice (P7 soma: MCPG, $t_5 = 1.07 \times 10^{-7}$, $P = 1.00$, suramin, $t_4 = 1.37$, $P = 0.24$, HC030031, $t_4 = 0.14$, $P = 0.89$; P30 soma: MCPG, $t_3 = 1.82$, $P = 0.17$, suramin, $t_3 = -1.26$, $P = 0.30$, HC030031, $t_5 = 2.70$, $P = 0.043$; P7 process: MCPG, $t_5 = 0.45$, $P = 0.67$, suramin, $t_4 = -1.19$, $P = 0.30$, HC030031, $t_4 = -2.41$, $P = 0.074$; P30 process: MCPG, $t_3 = 0.66$, $P = 0.56$, suramin, $t_3 = -1.44$, $P = 0.24$, HC030031, $t_5 = -0.90$, $P = 0.41$, paired t -test). Removal of extracellular Ca^{2+} significantly abolished astrocyte events at both soma and processes (Mann–Whitney U test, P7 soma: $P = 0.14$; P30 soma: $P = 0.0028$; P7 process: $P = 0.025$; P30 process: $P = 0.0070$).

Ongoing neuronal activity does not affect subcellular Ca^{2+} signals in astrocytes

To examine how astrocyte Ca^{2+} signals are affected by background neuronal activity, we tested the effect of tetrodotoxin (TTX), a voltage-sensitive sodium channel blocker (Fig. 5A). No significant changes in the frequencies of Ca^{2+} events were detected after application of TTX at both ages (P7 all events: $t_5 = -0.46$, $P = 0.67$; P30 all events: $t_3 = -0.54$, $P = 0.63$; P7 large events: $t_5 = 0.15$, $P = 0.89$; P30 large events: $t_3 = 2.33$, $P = 0.10$, paired t -test). These results demonstrate that sporadic subcellular activity is intrinsic to astrocytes and independent of neuronal spikes. Next, we examined whether naturally occurring synchronized activity of neuronal populations could influence astrocyte Ca^{2+} signals. As animals grow during the juvenile period, hippocampal neurons begin to spontaneously generate an organized network oscillation, termed a sharp-wave ripple complex (Buzsáki *et al.*, 1992), which apparently emerges in mice at more than 2 weeks after birth (Buhl & Buzsáki, 2005). This activity is one of the strongest network oscillations in

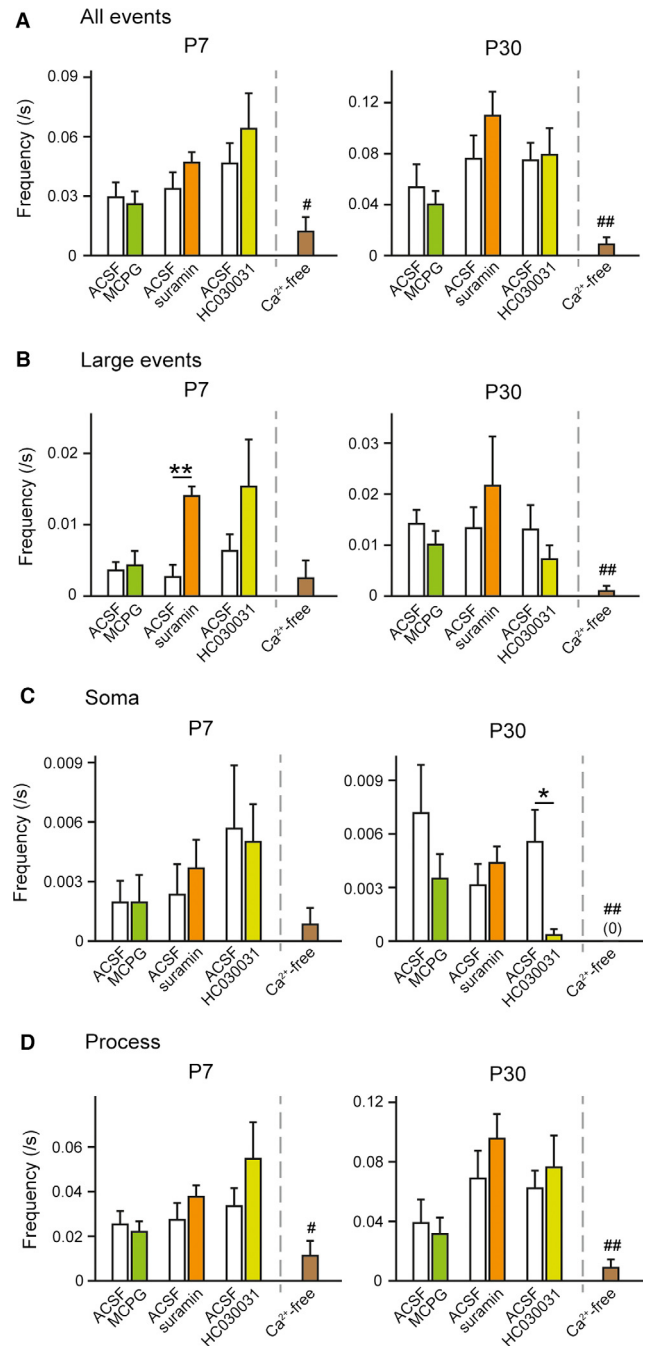


FIG. 4. Effects of pharmacological reagents on astrocyte events. (A) Average frequencies of all events before and after application of MCPG, a group I and II metabotropic glutamate receptor antagonist, suramin, a broad purinergic receptor antagonist, and HC030031, a TRPA1 channel antagonist. Paired t -test, $P > 0.05$. The frequency of all events observed in the Ca^{2+} -free aCSF condition was compared with that observed in the control condition shown in Fig. 2E. # $P < 0.05$, ## $P < 0.01$, Mann–Whitney U -test. (B) Same as in A but specifically analysed for large events with a size of $>100 \mu m^2$. Paired t -test, ** $P < 0.01$. (C, D) Same as in A but specifically analysed for events at soma (C) and processes (D). Paired t -test, * $P < 0.05$.

the brain and can transiently trigger action potentials in a large number of hippocampal pyramidal neurons. Because sharp waves (SPWs) spontaneously occur not only in *in vivo* animals but also in hippocampal slices, the observed increase in astrocyte Ca^{2+} signals in older mice might be explained by the presence of SPWs. The

slice was obtained by cutting the brain tissue at a specific angle so that the slice maintains more Schaffer collateral projections than conventional horizontal slices (Mizunuma *et al.*, 2014). To confirm SPW-induced neuronal activation, we first simultaneously performed LFP recordings from the CA1 stratum radiatum and multi-neuron

Ca²⁺ imaging from a neuronal population loaded with OGB-1 AM (Fig. 5B) (Miyawaki *et al.*, 2014). In slices at P30–40, spontaneous SPWs occurred intermittently at a rate of 0.2 Hz ($n = 8$ slices). The frequency of spike-associated Ca²⁺ transients increased by $1021 \pm 305\%$ at the peak time of the SPWs (Fig. 5C; $n = 619$ cells

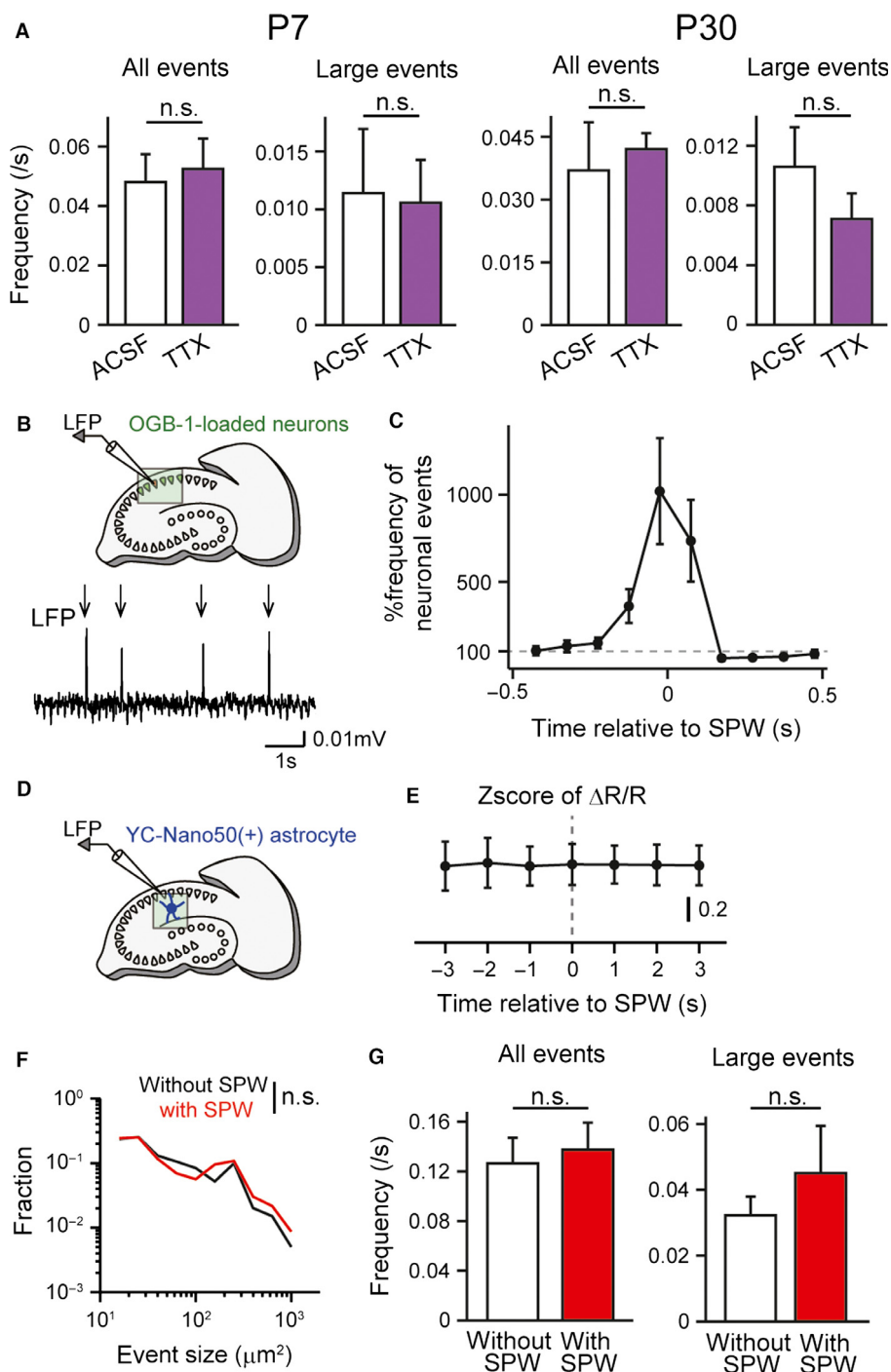


FIG. 5. Astrocyte Ca²⁺ signals are not affected by neuronal activity. (A) Average frequencies of all events and events with a size of $>100 \mu\text{m}^2$ before and after application of TTX. Paired *t*-test, $P > 0.05$. (B) Simultaneous recordings of extracellular LFP signals and spike-induced Ca²⁺ transients of OGB-1-loaded neurons in the hippocampal CA1 pyramidal cell layer. The bottom panel shows a representative LFP trace filtered at 2–30 Hz. Four SPWs are indicated by arrows. (C) SPW-triggered event rate of Ca²⁺ transients of OGB-1-loaded CA1 pyramidal neurons ($n = 619$ cells from 13 slices). The data were reproduced from Miyawaki *et al.* (2014). (D) During recording of extracellular LFP signal, the $\Delta R/R$ fluorescence trace was extracted from the entire structure of a single YC-Nano50-expressing astrocyte in the hippocampal CA1 stratum radiatum. (E) SPW-triggered average of $\Delta R/R$ fluorescence of an entire astrocyte image. (F) Size distribution of subcellular Ca²⁺ signals in astrocytes detected in frames with and without the emergence of SPWs. Kolmogorov–Smirnov test, $P > 0.05$. (G) Average frequency of all Ca²⁺ events (left) and large Ca²⁺ events with a size of $>100 \mu\text{m}^2$ (right) in frames with and without SPWs. Paired *t*-test, $P > 0.05$.

from 13 slices; data from Miyawaki *et al.*, 2014 were re-analysed). In SPW-positive slices, subcellular Ca²⁺ events were monitored from a single YC-Nano50-expressing astrocyte (Fig. 5D). The SPW-triggered average of $\Delta R/R$ intensity of the whole territory of a single astrocyte showed no pronounced changes in the signal amplitudes time-locked to the occurrence of SPWs (Fig. 5E). Correspondingly, no significant differences were observed in the distribution of event size, the frequency of all Ca²⁺ events and large Ca²⁺ events (>100 μm^2) between frames with and without the emergence of SPWs (Fig. 5F and G; size distribution, $D_{828} = 0.07$, $P = 0.32$; all events, $t_8 = 0.81$, $P = 0.44$; large events, $t_8 = 1.14$, $P = 0.29$, paired *t*-test). These results demonstrate that SPW generation, which strongly recruits neuronal synchronization, does not influence subcellular Ca²⁺ activity patterns in astrocytes.

Discussion

This study examined how subcellular Ca²⁺ activity patterns of astrocytes change with juvenile development. Using a wide-field confocal scanning technique that can capture the entire cell morphology of single astrocytes, we revealed that (1) astrocyte Ca²⁺ signals were not synchronous across multiple subcellular compartments, (2) Ca²⁺ events in P30 astrocytes are larger and more frequently occur at the somatic region than those in P7 astrocytes and (3) Ca²⁺ activity during the juvenile period is independent of the SPW-induced synchronized firing of neurons. We note that our imaging method with a 40 \times objective lens and a sampling rate of 1–5 Hz focused mainly on Ca²⁺ events that are larger than 16 μm^2 (100 pixels) might have overlooked millisecond-order and micrometre-order Ca²⁺ events localized in microscopic parts of astrocytic processes (Di Castro *et al.*, 2011; Panatier *et al.*, 2011); however, the tradeoff of the spatial and temporal resolution revealed the novel phenomena at a systematic cellular level.

Using an ROI-free analysis, the size distribution plotted in double-logarithmic coordinates revealed that astrocyte Ca²⁺ events were not separated into discrete groups but rather collapsed onto a relationship that resembles a power-law probability distribution, corresponding to a previous finding (Wu *et al.*, 2014). As represented in the tail of the distribution, astrocytes occasionally emitted expanded Ca²⁺ events of large size (>100 μm^2) and long duration (>10 s), which widely spread across multiple branches. The global signal is probably an efficient signal to cover multiple functional microdomains and may exert regulatory effects simultaneously on thousands of synapses. On the other hand, more than 80% of events had a size of <100 μm^2 with a duration of <1 s. Assuming that these localized events are sufficient to represent spontaneous neurotransmission at a single synapse and independently regulate neighbouring synapses (Di Castro *et al.*, 2011; Panatier *et al.*, 2011; Volterra *et al.*, 2014), our data indicate that astrocytic fine processes may be more active and more frequently participate in the local modulation of synaptic function than previously thought.

The size increase in the rat brain is largely governed by an increase in the number of glial cells and an expansion of both neurons and glial cells. In the developing hippocampus, the volume of astrocytes increases with a prominent elaboration of spongiform processes throughout the first month (Bushong *et al.*, 2004). During this growing period, the expression patterns of a variety of functional proteins in astrocytes, such as the glutamate transporter (Sutherland *et al.*, 1996; Furuta *et al.*, 1997), connexin (Nagy *et al.*, 1999), metabotropic glutamate receptors (Sun *et al.*, 2013) and potassium channels (Seifert *et al.*, 2009), have been shown to undergo dynamic changes, which would lead to changes in astrocyte Ca²⁺ signals during development.

Our analyses revealed that the size of astrocyte subcellular Ca²⁺ events increases with morphological maturation from postnatal weeks 1 to 4. This developmental pattern may represent an efficient property of astrocytes to invariantly support and maintain the same sets of synapses and blood vessels against developmental increases in brain size. Our pharmacological experiments indicate that extracellular Ca²⁺ influx, rather than metabotropic glutamate receptors, purinergic receptors, is a major source of astrocyte Ca²⁺ activity at both soma and processes. These results are consistent with the recent finding that knockout of IP3 type2 receptor enriched in astrocytes had little effect on Ca²⁺ signals especially at fine microdomain processes, which indicates extracellular Ca²⁺ influx is a trigger for the localized Ca²⁺ events (Srinivasan *et al.*, 2015). In addition, a previous study has shown that activation of TRPA1 channels is also involved in astrocyte Ca²⁺ events in juvenile mice (Shigetomi *et al.*, 2012). Our result showed that the TRPA1-dependent Ca²⁺ events occurred more frequently in the soma than processes especially in late juvenile mice. Further studies are needed to clarify the detailed mechanisms that are upstream and downstream of these pathways.

We failed to observe that ongoing generation of SPWs, a typical synchronized activity of neurons, affects the spatiotemporal patterns of astrocyte Ca²⁺ events. This is not due to insensitivity of the Ca²⁺ sensor because we detected apparent Ca²⁺ responses against burst electrical stimulation, as shown in Fig. 1D, consistent with previous studies (Porter & McCarthy, 1996; Perea & Araque, 2005; Gordon *et al.*, 2009; Tang *et al.*, 2015). The difference between naturally occurring SPWs and the conventional artificial stimulation is that SPWs trigger synchronous but spatially sparse firing of a subset of cells (Ylinen *et al.*, 1995; Csicsvari *et al.*, 2000; Mizunuma *et al.*, 2014) whereas the stimulation protocol intensely triggers firing of spatially localized afferent fibres. Our observation questions the idea that naturally occurring neuronal synchronization is a major source of astrocyte Ca²⁺ activity, implicated by previous studies with artificial stimulation protocols.

As reviewed in a recent paper (Volterra *et al.*, 2014), astrocyte subcellular Ca²⁺ signals appear highly complex. The developmental maturation of astrocyte Ca²⁺ signals in parallel with the elaboration of astrocytic ramified processes may promote intricate interactions between neurons and astrocytes to establish organized circuits in brain systems.

Conflict of interests

The authors declare no conflict of interest.

Acknowledgements

This work was supported by Kaken-hi (22115003; 2625000), The Takeda Science Foundation, The Research Foundation for Pharmaceutical Sciences and The Kobayashi International Scholarship Foundation. We thank Dr Kazunori Kanemaru for providing transgenic mice and antibody, Dr Ryuta Koyama for teaching us the mouse slice culture technique and Takeyuki Miyawaki for providing sharp wave data.

Abbreviations

aCSF, artificial cerebrospinal fluid; CFP, cyan fluorescent protein; Div, days *in vitro*; GECl, genetically encoded Ca²⁺ indicator; GFAP, glial fibrillary acidic protein; LFP, local field potential; MCPG, methyl-(4-carboxyphenyl) glycine; Mlc-1, megalencephalic leukoencephalopathy with subcortical cysts 1; OGB-1, Oregon Green 488 BAPTA-1; PBS, phosphate buffered saline; PFA, paraformaldehyde; ROI, region of interest; SPW, sharp wave; TRPA1, transient receptor potential ankyrin-1; TTX, tetrodotoxin; YC-Nano50, Yellow Cameleon-Nano50; YFP, yellow fluorescent protein.

References

- Agulhon, C., Fiocco, T.A. & McCarthy, K.D. (2010) Hippocampal short- and long-term plasticity are not modulated by astrocyte Ca^{2+} signaling. *Science*, **327**, 1250–1254.
- Asada, A., Ujita, S., Nakayama, R., Oba, S., Ishii, S., Matsuki, N. & Ikegaya, Y. (2015) Subtle modulation of ongoing calcium dynamics in astrocytic microdomains by sensory inputs. *Physiol. Rep.*, **3**, e12454.
- Attwell, D., Buchan, A.M., Charpak, S., Lauritzen, M., Macvicar, B.A. & Newman, E.A. (2010) Glial and neuronal control of brain blood flow. *Nature*, **468**, 232–243.
- Buhl, D.L. & Buzsaki, G. (2005) Developmental emergence of hippocampal fast-field “ripple” oscillations in the behaving rat pups. *Neuroscience*, **134**, 1423–1430.
- Bushong, E.A., Martone, M.E., Jones, Y.Z. & Ellisman, M.H. (2002) Protoplasmic astrocytes in CA1 stratum radiatum occupy separate anatomical domains. *J. Neurosci.*, **22**, 183–192.
- Bushong, E.A., Martone, M.E. & Ellisman, M.H. (2004) Maturation of astrocyte morphology and the establishment of astrocyte domains during postnatal hippocampal development. *Int. J. Dev. Neurosci.*, **22**, 73–86.
- Buzsaki, G., Horvath, Z., Urioste, R., Hetke, J. & Wise, K. (1992) High-frequency network oscillation in the hippocampus. *Science*, **256**, 1025–1027.
- Csicsvari, J., Hirase, H., Mamiya, A. & Buzsaki, G. (2000) Ensemble patterns of hippocampal CA3-CA1 neurons during sharp wave-associated population events. *Neuron*, **28**, 585–594.
- Di Castro, M.A., Chuquet, J., Liaudet, N., Bhaukaurally, K., Santello, M., Bouvier, D., Tiret, P. & Volterra, A. (2011) Local Ca^{2+} detection and modulation of synaptic release by astrocytes. *Nat. Neurosci.*, **14**, 1276–1284.
- Fiocco, T.A., Agulhon, C. & McCarthy, K.D. (2009) Sorting out astrocyte physiology from pharmacology. *Annu. Rev. Pharmacol. Toxicol.*, **49**, 151–174.
- Freeman, M.R. (2010) Specification and morphogenesis of astrocytes. *Science*, **330**, 774–778.
- Furuta, A., Rothstein, J.D. & Martin, L.J. (1997) Glutamate transporter protein subtypes are expressed differentially during rat CNS development. *J. Neurosci.*, **17**, 8363–8375.
- Girouard, H., Bonev, A.D., Hannah, R.M., Meredith, A., Aldrich, R.W. & Nelson, M.T. (2010) Astrocytic endfoot Ca^{2+} and BK channels determine both arteriolar dilation and constriction. *Proc. Natl. Acad. Sci. USA*, **107**, 3811–3816.
- Gordon, G.R., Choi, H.B., Rungta, R.L., Ellis-Davies, G.C. & MacVicar, B.A. (2008) Brain metabolism dictates the polarity of astrocyte control over arterioles. *Nature*, **456**, 745–749.
- Gordon, G.R., Iremonger, K.J., Kantevari, S., Ellis-Davies, G.C., MacVicar, B.A. & Bains, J.S. (2009) Astrocyte-mediated distributed plasticity at hypothalamic glutamate synapses. *Neuron*, **64**, 391–403.
- Haustein, M.D., Kracun, S., Lu, X.H., Shih, T., Jackson-Weaver, O., Tong, X., Xu, J., Yang, X.W., O’Dell, T.J., Marvin, J.S., Ellisman, M.H., Bushong, E.A., Looger, L.L. & Khakh, B.S. (2014) Conditions and constraints for astrocyte calcium signaling in the hippocampal mossy fiber pathway. *Neuron*, **82**, 413–429.
- Horikawa, K., Yamada, Y., Matsuda, T., Kobayashi, K., Hashimoto, M., Matsu-ura, T., Miyawaki, A., Michikawa, T., Mikoshiba, K. & Nagai, T. (2010) Spontaneous network activity visualized by ultrasensitive Ca^{2+} indicators, yellow Cameleon-Nano. *Nat. Methods*, **7**, 729–732.
- Kanemaru, K., Sekiya, H., Xu, M., Satoh, K., Kitajima, N., Yoshida, K., Okubo, Y., Sasaki, T., Moritoh, S., Hasuwa, H., Mimura, M., Horikawa, K., Matsui, K., Nagai, T., Iino, M. & Tanaka, K.F. (2014) *In vivo* visualization of subtle, transient, and local activity of astrocytes using an ultrasensitive Ca^{2+} indicator. *Cell Rep.*, **8**, 311–318.
- Khakh, B.S. & McCarthy, K.D. (2015) Astrocyte calcium signaling: from observations to functions and the challenges therein. *Cold Spring Harb. Perspect. Biol.*, **7**, a020404.
- Min, R. & Nevian, T. (2012) Astrocyte signaling controls spike timing-dependent depression at neocortical synapses. *Nat. Neurosci.*, **15**, 746–753.
- Miyawaki, T., Norimoto, H., Ishikawa, T., Watanabe, Y., Matsuki, N. & Ikegaya, Y. (2014) Dopamine receptor activation reorganizes neuronal ensembles during hippocampal sharp waves *in vitro*. *PLoS One*, **9**, e104438.
- Mizunuma, M., Norimoto, H., Tao, K., Egawa, T., Hanaoka, K., Sakaguchi, T., Hioki, H., Kaneko, T., Yamaguchi, S., Nagano, T., Matsuki, N. & Ikegaya, Y. (2014) Unbalanced excitability underlies offline reactivation of behaviorally activated neurons. *Nat. Neurosci.*, **17**, 503–505.
- Nagy, J.I., Patel, D., Ochalski, P.A. & Stelmack, G.L. (1999) Connexin30 in rodent, cat and human brain: selective expression in gray matter astrocytes, co-localization with connexin43 at gap junctions and late developmental appearance. *Neuroscience*, **88**, 447–468.
- Panatier, A., Vallee, J., Haber, M., Murai, K.K., Lacaillle, J.C. & Robitaille, R. (2011) Astrocytes are endogenous regulators of basal transmission at central synapses. *Cell*, **146**, 785–798.
- Perea, G. & Araque, A. (2005) Properties of synaptically evoked astrocyte calcium signal reveal synaptic information processing by astrocytes. *J. Neurosci.*, **25**, 2192–2203.
- Porter, J.T. & McCarthy, K.D. (1996) Hippocampal astrocytes *in situ* respond to glutamate released from synaptic terminals. *J. Neurosci.*, **16**, 5073–5081.
- Reeves, A.M., Shigetomi, E. & Khakh, B.S. (2011) Bulk loading of calcium indicator dyes to study astrocyte physiology: key limitations and improvements using morphological maps. *J. Neurosci.*, **31**, 9353–9358.
- Schmitt, A., Gofferje, V., Weber, M., Meyer, J., Mossner, R. & Lesch, K.P. (2003) The brain-specific protein MLC1 implicated in megalencephalic leukoencephalopathy with subcortical cysts is expressed in glial cells in the murine brain. *Glia*, **44**, 283–295.
- Seifert, G., Huttmann, K., Binder, D.K., Hartmann, C., Wyczynski, A., Neusch, C. & Steinhilber, C. (2009) Analysis of astroglial K^{+} channel expression in the developing hippocampus reveals a predominant role of the Kir4.1 subunit. *J. Neurosci.*, **29**, 7474–7488.
- Shigetomi, E., Kracun, S., Sofroniew, M.V. & Khakh, B.S. (2010) A genetically targeted optical sensor to monitor calcium signals in astrocyte processes. *Nat. Neurosci.*, **13**, 759–766.
- Shigetomi, E., Tong, X., Kwan, K.Y., Corey, D.P. & Khakh, B.S. (2012) TRPA1 channels regulate astrocyte resting calcium and inhibitory synapse efficacy through GAT-3. *Nat. Neurosci.*, **15**, 70–80.
- Srinivasan, R., Huang, B.S., Venugopal, S., Johnston, A.D., Chai, H., Zeng, H., Golshani, P. & Khakh, B.S. (2015) Ca^{2+} signaling in astrocytes from *Ip3r2^{-/-}* mice in brain slices and during startle responses *in vivo*. *Nat. Neurosci.*, **18**, 708–717.
- Sun, W., McConnell, E., Pare, J.F., Xu, Q., Chen, M., Peng, W., Lovatt, D., Han, X., Smith, Y. & Nedergaard, M. (2013) Glutamate-dependent neuroglial calcium signaling differs between young and adult brain. *Science*, **339**, 197–200.
- Sutherland, M.L., Delaney, T.A. & Noebels, J.L. (1996) Glutamate transporter mRNA expression in proliferative zones of the developing and adult murine CNS. *J. Neurosci.*, **16**, 2191–2207.
- Tanaka, K.F., Ahmari, S.E., Leonardo, E.D., Richardson-Jones, J.W., Budreck, E.C., Scheiffele, P., Sugio, S., Inamura, N., Ikenaka, K. & Hen, R. (2010) Flexible Accelerated STOP Tetracycline Operator-knockin (FAST): a versatile and efficient new gene modulating system. *Biol. Psychiatry*, **67**, 770–773.
- Tang, W., Szokol, K., Jensen, V., Enger, R., Trivedi, C.A., Hvalby, O., Helm, P.J., Looger, L.L., Sprengel, R. & Nagelhus, E.A. (2015) Stimulation-evoked Ca^{2+} signals in astrocytic processes at hippocampal CA3-CA1 synapses of adult mice are modulated by glutamate and ATP. *J. Neurosci.*, **35**, 3016–3021.
- Volterra, A., Liaudet, N. & Savtchouk, I. (2014) Astrocyte Ca^{2+} signalling: an unexpected complexity. *Nat. Rev. Neurosci.*, **15**, 327–335.
- Wu, Y.W., Tang, X., Arizono, M., Bannai, H., Shih, P.Y., Dembitskaya, Y., Kazantsev, V., Tanaka, M., Itoharu, S., Mikoshiba, K. & Semyanov, A. (2014) Spatiotemporal calcium dynamics in single astrocytes and its modulation by neuronal activity. *Cell Calcium*, **55**, 119–129.
- Ylinen, A., Bragin, A., Nadasdy, Z., Jando, G., Szabo, I., Sik, A. & Buzsaki, G. (1995) Sharp wave-associated high-frequency oscillation (200 Hz) in the intact hippocampus: network and intracellular mechanisms. *J. Neurosci.*, **15**, 30–46.